UDK 669.721.5:620.193
Original scientific article/Izvirni znanstveni članek

ISSN 1580-2949
Mater. Tehnol.

STUDY ON THE ELECTROCHEMICAL CORROSION BEHAVIOR OF Mg-xSn-0.6Ca (x = 1, 2, 6, 7) ALLOYS

ŠTUDIJ ELEKTROKEMIJSKEGA KOROZIJSKEGA OBNAŠANJA ZLITIN TIPA Mg-xSn-0,6Ca (x = 1, 2, 6, 7)

Tingting Song[1], Fu Yang[1], Xiaowei Niu[2], Zheng Jia[1,2,*]

[1]College of Mechanical Engineering, Shenyang University, Shenyang 110044, China
[2]College of Environment, Liaoning Province Pollution Environmental Remediation Professional Technology Innovation Center & Shenyang Key Laboratory of Collaborative Technology Innovation for Industrial Pollution Reduction and Carbon Reduction, Shenyang University, Shenyang 110044, China

Prejem rokopisa – received: 2025-06-28; sprejem za objavo – accepted for publication: 2026-01-23

doi:10.17222/mit.2025.1507

This study systematically investigated the effects of different Sn contents on the microstructure and electrochemical corrosion behavior of Mg-xSn-0.6Ca (x = 1, 2, 6, 7) alloys. The corrosion behavior of the alloys in a 3.5 *w*/% NaCl solution was evaluated using hydrogen evolution weight loss analysis, potentiodynamic polarization curve analysis, and electrochemical impedance spectroscopy (EIS). The results indicate that as the Sn content increases, the quantity and size of the Mg_2Sn and CaMgSn secondary phases in the alloys significantly increase, effectively hindering the diffusion of corrosive media, thereby enhancing the corrosion resistance of the alloys. When the Sn content is 6 %, the Mg-6Sn-0.6Ca alloy exhibits the best corrosion resistance. Electrochemical test results show that the Mg-6Sn-0.6Ca alloy has the lowest self-corrosion current density. Additionally, scanning electron microscope (SEM) and energy dispersive spectrometer (EDS) analyses reveal that the synergistic effect of Sn and Ca elements significantly improves the corrosion resistance of the alloy. However, an excessive Sn content (e.g., 7 %) may lead to localized micro-galvanic corrosion, reducing the corrosion resistance.

Keywords: Mg-Sn alloy, corrosion performance, electrochemistry, microstructure

Avtorji v članku opisujejo študijo, v kateri so sistematično raziskali vplive različnih vsebnosti kositra (Sn) na mikrostrukturo in elektrokemijsko korozijsko obnašanje zlitin tipa Mg-xSn-0,6Ca (x = 1, 2, 6, 7). Korozijsko obnašanje zlitin v 3,5 *w*/% raztopini NaCl so ocenili s pomočjo analize izgube na masi zaradi sproščanja vodika, analizo potenciodinamične polarizacijske krivulje in elektrokemijsko impedančno spektroskopijo (EIS). Rezultati so pokazali, da se z naraščanjem vsebnosti Sn znatno povečata količina in velikost sekundarnih faz Mg_2Sn in CaMgSn v zlitinah, kar učinkovito ovira difuzijo korozivnih medijev in s tem povečuje korozijsko odpornost zlitin. Ko je vsebnost Sn 6 %, ima zlitina Mg-6Sn-0,6Ca najboljšo korozijsko odpornost. Rezultati elektrokemijskih testov so pokazali, da ima zlitina Mg-6Sn-0,6Ca najnižjo gostoto samokorozijskega toka. Poleg tega analize z vrstičnim elektronskim mikroskopom (SEM) in energijsko disperzijskim spektrometrom (EDS) kažejo, da učinek vzajemnega delovanja Sn in Ca znatno izboljša korozijsko odpornost zlitine. Vendar pa lahko prekomerna vsebnost Sn (npr. 7 %) povzroči lokalno mikrogalvansko korozijo, kar zmanjša odpornost proti koroziji.

Ključne besede: zlitina Mg-Sn-Ca, odpornost proti koroziji, elektrokemija, mikrostruktura

1 INTRODUCTION

Magnesium alloys have become a focal point in lightweight material research due to their properties such as low density and high strength. However, their corrosion resistance remains a significant challenge. Common methods to enhance corrosion resistance include chemical conversion coatings, electrochemical plating, anodizing, the addition of corrosion inhibitors, and alloying. Among these, alloying is widely adopted due to its relatively simple preparation process.[1–10] Alloying can fundamentally improve the corrosion resistance of magnesium alloys.

Sn and Ca, common alloying elements, have been proven to effectively enhance the corrosion resistance of magnesium alloys. The addition of Sn can improve the strength and corrosion resistance of an alloy by forming the Mg_2Sn phase.[11] Furthermore, the addition of Ca can form thermally stable CaMgSn phases, further enhancing the corrosion resistance of an alloy.[12] Zang[13] found that Ca not only forms a dense oxide film to prevent the penetration of external media, but the addition of a small amount of Ca can also shift the corrosion mode of magnesium alloys from pitting corrosion to filiform corrosion. Recent studies have shown that the addition of an appropriate amount of Ca can improve the corrosion resistance of magnesium alloys by forming protective films and refining grain structures. However, the mechanism by which the Sn content influences the corrosion behavior of Mg-Sn-Ca alloys remains unclear, particularly the effects of different Sn contents on the microstructure, distribution of secondary phases, and electrochemical corrosion behavior of the alloys, which still require in-depth investigation.

*Corresponding author's e-mail:
jz140@163.com (Zheng Jia)

This study focuses on Mg-xSn-0.6Ca (x = 1, 2, 6, 7) alloys as the research subject. By adjusting the Sn content, the influence of Sn on the microstructure, distribution of secondary phases, and electrochemical corrosion behavior of the alloys is systematically investigated. The corrosion mechanisms are explored to reveal the impact of Sn content on the corrosion behavior of the alloys. The aim is to provide theoretical insights and experimental foundations for the development of novel corrosion-resistant magnesium alloys.

2 EXPERIMENTAL METHODS

Using industrial pure Mg (99.9 *w*/%), pure Sn (99.9 *w*/%), and the intermediate alloy Mg-25 %Ca as raw materials, the Mg-xSn-0.6Ca (x = 1, 2, 6, 7) alloys were prepared by melting in an S62-12-9 crucible-type resistance furnace. During the melting process, the yield of pure Mg was 97 %, and the loss of other elements was negligible. Subsequently, the alloys underwent a 12-hour homogenization treatment and were cut into (10 × 10 × 10) mm samples for further use.

The phase composition of the alloys was analyzed using an X-ray diffractometer (XRD), and the data were processed using MDI Jade 9.0 software. The alloy samples were ground and polished with sandpaper. Grain boundary etching was performed using a picric acid solution (4.2 g picric acid + 10 mL deionized water + 70 mL ethanol + 10 mL acetic acid). The microstructure was observed using a scanning electron microscope (SEM), and the chemical composition of the secondary phases was analyzed using an energy dispersive spectrometer (EDS).

The polished samples were immersed in a 3.5 *w*/% NaCl solution for 24 h, then removed, rinsed with distilled water and alcohol, and dried. For the study of surface films, the samples were directly sputter-coated with gold and observed using SEM. For the investigation of corrosion morphology, the corrosion products were removed using a chromic acid solution (180 g/L CrO_3), followed by SEM observation.

The samples were encapsulated in epoxy resin, leaving a (10 × 10) mm working surface exposed. The samples were then immersed in a 3.5 *w*/% NaCl solution for 24 h, after which the corrosion products were removed using a chromic acid solution, and the hydrogen evolution weight loss rate was calculated.

The Equation for calculating the hydrogen evolution corrosion rate is as follows:[14]

$$P_{\mathrm{H}} = \frac{8.76 \cdot 10^4 \times \Delta V \times M}{A \times T \times \rho} \tag{1}$$

In the Equation: P_{H}: corrosion rate from hydrogen evolution testing, mm·year^{-1}; ΔV: total volume of hydrogen gas evolved during the hydrogen evolution test, mL; M: the relationship between the hydrogen generation rate and the mass loss rate of the alloy, with a value of 0.001083, g·mL^{-1}; A: total surface area of the hydrogen evolution sample, cm^2; t: immersion time of the hydrogen evolution test, h; ρ: density of the alloy sample, g·cm^{-3}.

The Equation for calculating the weight loss corrosion rate is as follows:[15]

$$P_{\mathrm{W}} = \frac{8.76 \cdot 10^4 \times \Delta g}{A \times T \times \rho} \tag{2}$$

In the Equation: P_{W}: corrosion rate from weight loss testing, mm·year^{-1}; Δg: mass difference of the alloy before and after the weight loss test, g; A: total surface area of the weight loss sample, cm^2; t: corrosion time, h; ρ: density of the alloy sample, g·cm^{-3}.

The electrochemical test samples were also encapsulated in epoxy resin, leaving a (10 × 10) mm working surface exposed and connecting electrode leads. The samples were ground and polished, and a three-electrode system was employed: the working electrode was the sample, the counter electrode was a Pt sheet, and the reference electrode was a saturated calomel electrode (SCE). The tests were conducted using an electrochemical workstation (CHI660E model) with a 3.5 *w*/% NaCl solution as the corrosion medium.

First, the test samples were immersed in the 3.5 *w*/% NaCl solution and allowed to stabilize for 3600 s to measure the open circuit potential (OCP). Subsequently, electrochemical impedance spectroscopy (EIS) tests were performed in a frequency range of 0.01 Hz to 1 MHz, and the obtained data were fitted and analyzed using Zview software. For the potentiodynamic polarization tests, a potential window of ±0.5 V relative to the instantaneous potential was set, and a constant scan rate of 1 mV/s was applied. Finally, the Tafel extrapolation method was used to extract key parameters such as the corrosion potential (ecorr) and corrosion current density (icorr) of the experimental alloys from the polarization curves.

3 RESULTS

Figure 1 displays the microstructures of homogenized Mg-1Sn-0.6Ca, Mg-2Sn-0.6Ca, Mg-6Sn-0.6Ca, and Mg-7Sn-0.6Ca alloys. As shown in the figure, a large number of secondary phases are present in the homogenized alloys, with their sizes ranging from tens to hundreds of micrometers. Higher magnification images further reveal that, in addition to the typical skeletal secondary phases in the eutectic structure, there is also a strip-like secondary phase. As the Sn content increases, the contrast of the secondary phase structure gradually intensifies, and the number of strip-like secondary phases significantly increases, indicating that variations in the Sn content have a notable impact on the evolution of secondary phases in the alloys.

Based on the EDS analysis results presented in **Table 1**, it can be determined that the skeletal secondary

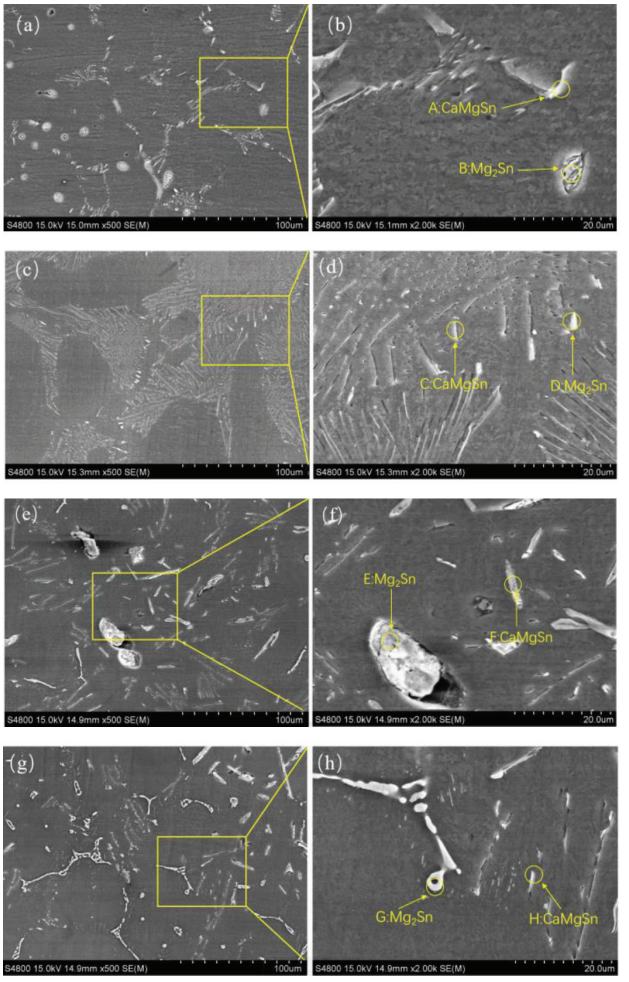

Figure 1: SEM micrographs of the homogenized alloys: a), b) Mg-1Sn-0.6Ca; c), d) Mg-2Sn-0.6Ca; e), f) Mg-6Sn-0.6Ca; g), h) Mg-7Sn-0.6Ca

Table 1: EDS analysis of the precipitated phases in the alloys shown in **Figure 1** (φ/%)

Marked points	Chemical composition, φ/%			Phase composition
	Mg	Sn	Ca	
A	93.27	3.91	2.82	CaMgSn
B	77.47	21.79	0.74	Mg_2Sn
C	88.72	6.02	.26	CaMgSn
D	73.63	25.71	0.66	Mg_2Sn
E	71.42	27.77	0.81	Mg_2Sn
F	79.26	11.12	9.62	CaMgSn
G	74.50	25.32	0.17	Mg_2Sn
H	89.57	5.99	4.44	CaMgSn

phase is the Mg_2Sn phase, while the strip-like secondary phase is the CaMgSn phase. This finding is consistent with the research of Qiu et al.,[11] who noted that the formation of the Mg_2Sn phase can effectively enhance the strength and corrosion resistance of an alloy. The presence of the CaMgSn phase promotes the formation of a denser and more stable oxide film on the surface of a magnesium alloy, thereby improving its corrosion resistance. Wang[16] pointed out that the CaMgSn phase can act as a cathodic phase during the corrosion process, facilitating the formation of a protective oxide film in the anodic region, thus inhibiting further corrosion propagation.

Figure 2 shows the XRD patterns of the homogenized alloys. XRD can accurately identify the presence and relative content of different phases by detecting diffraction peaks of crystal structures in the material. The intensity of the diffraction peaks is proportional to the quantity and size of the corresponding phases. Therefore, by analyzing the changes in diffraction peaks, the quantity and size of secondary phases can be inferred. As seen in the figure, the alloy samples exhibit multiple diffraction peaks corresponding to intermetallic compounds formed between Mg and alloying elements. Other diffraction peaks in the patterns correspond to intermetallic compounds such as Mg_2Sn and CaMgSn, confirming the presence of secondary phases in the alloys. With the increase in Sn, the diffraction peak intensity of the Mg_2Sn phase significantly increases, indicating that a higher Sn content promotes the formation and growth of the Mg_2Sn phase. Similarly, changes in diffraction peak intensity reflect variations in the quantity and size of secondary phases. The higher the Sn content, the greater the quantity and size of the secondary phases.

Figure 3a shows the hydrogen evolution curves of the four alloys immersed in the 3.5 *w*/% NaCl solution for 24 h. The results indicate that the hydrogen evolution volume of all alloys increases linearly over time. Among them, Mg-1Sn-0.6Ca exhibits the highest hydrogen evolution volume and rate, indicating the poorest corrosion resistance, while Mg-6Sn-0.6Ca shows the lowest hydrogen evolution volume and rate, demonstrating the best corrosion resistance. **Figure 3b** presents the hydrogen evolution weight loss rates of the homogenized alloys, revealing that the corrosion resistance of the alloys initially improves and then deteriorates with increasing Sn content. The average hydrogen evolution rate (PH) and weight loss corrosion rate (Pw) for Mg-1Sn-0.6Ca are

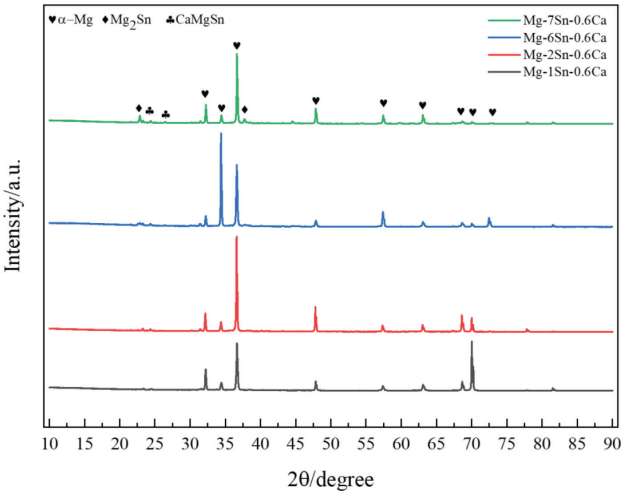

Figure 2: XRD patterns of the homogenized alloys

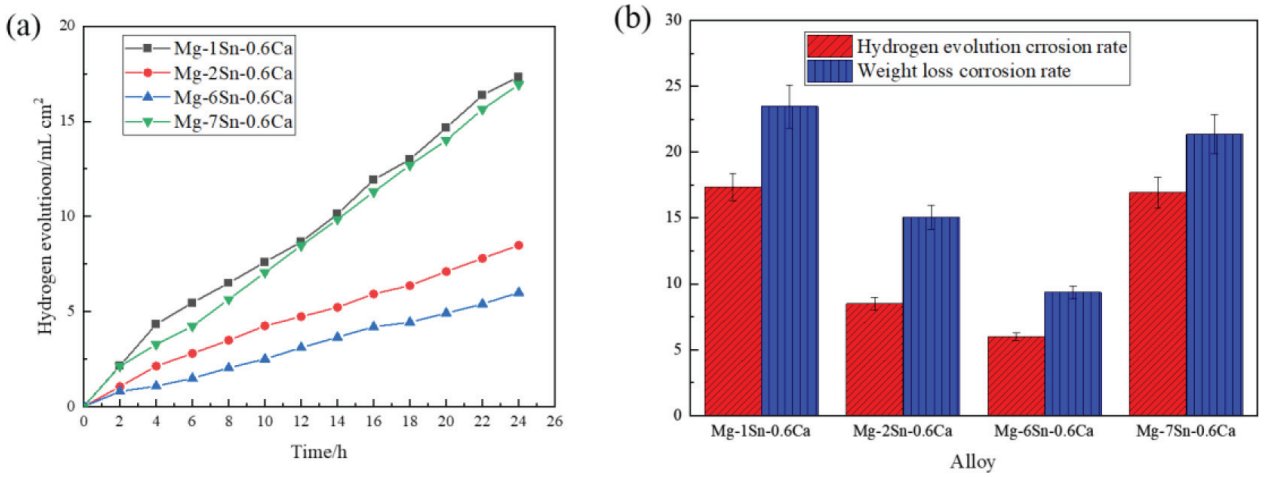

Figure 3: Corrosion behavior of the homogenized experimental alloys in 3.5 *w*/% NaCl solution: a) hydrogen evolution volume vs. time curves; b) hydrogen evolution and weight loss corrosion rates

17.339 mm·year^{-1} and 23.468 mm·year^{-1}, respectively; for Mg-2Sn-0.6Ca, they are 8.486 mm·year^{-1} and 15.064 mm·year^{-1}; for Mg-6Sn-0.6Ca, they are 5.999 mm·year^{-1} and 9.346 mm·year^{-1}; and for Mg-7Sn-0.6Ca, they are 16.93 mm·year^{-1} and 21.35 mm·year^{-1}. When the Sn content is 6 %, the Mg-6Sn-0.6Ca alloy exhibits the optimal corrosion resistance. Compared to the Mg-1Sn-0.6Ca alloy, which has the poorest corrosion resistance, the hydrogen evolution rate and weight loss corrosion rate of Mg-6Sn-0.6Ca are reduced by 65.4 % and 60.2 %, respectively, showing significant improvement.

Figure 4 shows the potentiodynamic polarization curves of the homogenized alloys after electrochemical testing in the 3.5 *w*/% NaCl solution, with the curves fitted using the Tafel extrapolation method. The corrosion potential (ecorr) and corrosion current density (i_{corr}) obtained from the fitting results are listed in **Table 3**. As seen in **Figure 4**, the polarization curves of the five experimental alloys exhibit asymmetric cathodic and anodic branches. From a thermodynamic perspective, the corrosion potential (e_{corr}) is a thermodynamic parameter that indicates the tendency of alloy corrosion. The figure reveals that, compared to the Mg-6Sn-0.6Ca alloy, the corrosion potentials of the Mg-1Sn-0.6Ca, Mg-2Sn-0.6Ca, and Mg-7Sn-0.6Ca alloys shift downward, suggesting an increased thermodynamic tendency for corrosion in these alloys. However, studies have shown that the corrosion current density (icorr) reflects the actual corrosion rate of an alloy.[17] According to Faraday's law of electrolysis, the corrosion rate of a metal is directly proportional to the corrosion current density, meaning that a lower corrosion current density corresponds to a lower corrosion rate and better corrosion resistance.[18,19] The experimental results indicate that the corrosion current densities of the four homogenized alloys – Mg-1Sn-0.6Ca, Mg-2Sn-0.6Ca, Mg-6Sn-0.6Ca, and Mg-7Sn-0.6Ca – are 12.45 μA·cm^{-2}, 9.32 μA·cm^{-2}, 9.17 μA·cm^{-2}, and 9.61 μA·cm^{-2}, respectively. This demonstrates that the Mg-6Sn-0.6Ca alloy exhibits the best corrosion resistance, which is consistent with the hydrogen evolution and weight loss results.

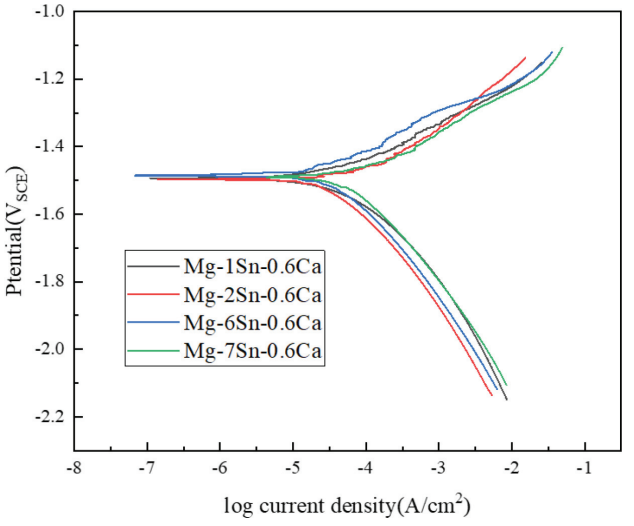

Figure 4: Polarization curves of the homogenized alloys

Table 2: Fitting results of the polarization curves for the homogenized alloys

Alloys	e_{corr}/V	i_{corr}/μA·cm^{-2}	p_i/mm·year^{-1}
Mg-1Sn-0.6Ca	–1.494	12.45	0.28
Mg-2Sn-0.6Ca	–1.497	9.32	0.21
Mg-6Sn-0.6Ca	–1.486	9.17	0.21
Mg-7Sn-0.6Ca	–1.491	9.61	0.22

To more accurately analyze the corrosion process of the experimental alloys, the negative difference effect that may occur during the corrosion of magnesium alloys and the complexity of the electrochemical corrosion process were considered. Relying solely on a single polarization curve cannot fully reflect the actual corrosion behavior of the alloys. Therefore, electrochemical impedance spectroscopy (EIS) analysis was performed on the homogenized experimental alloys in the 3.5 *w*/%

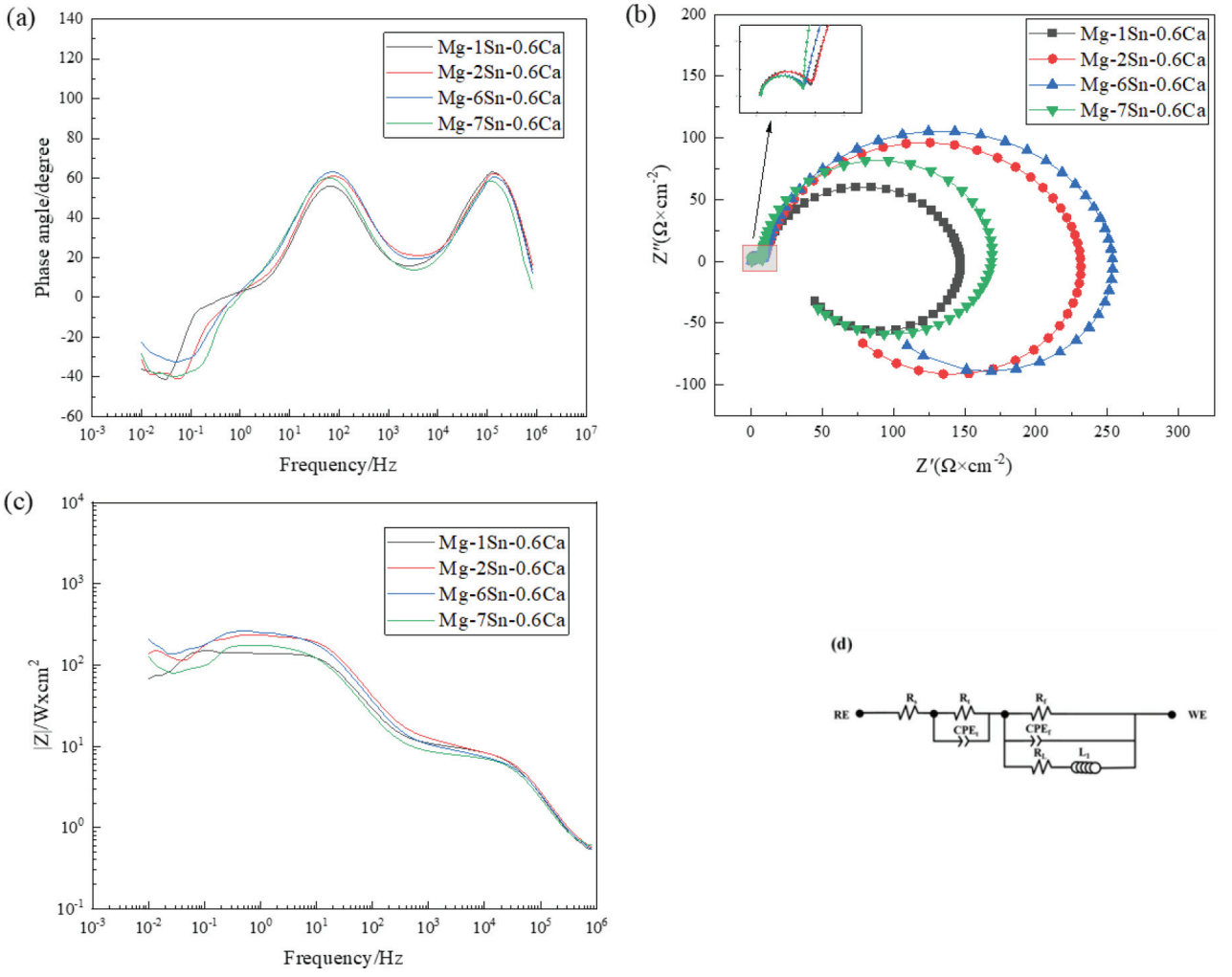

Figure 5: Electrochemical impedance spectra of the homogenized alloys in 3.5 *w*/% NaCl solution: a) phase angle plot; b) Nyquist plot; c) Bode plot; d) equivalent circuit diagram

NaCl solution, and the results are shown in **Figure 5**. The peaks in the phase angle-frequency curve in **Figure 5a** can be used to determine the time constants of the impedance spectra and to identify whether they act as resistive or capacitive components in the electrode, thereby enabling the construction of the equivalent circuit diagram shown in **Figure 5d**. The impedance spectra were fitted based on this circuit diagram, and the results are presented in **Table 2**. Here, Rs represents the solution resistance, Rt represents the charge transfer resistance, CPEt represents the double-layer capacitance, Rf represents the surface film resistance, and CPEf is the surface film capacitance. From the phase angle-frequency curve in **Figure 5a**, it can be observed that all five alloys exhibit two peaks, indicating two time constants in the electrochemical impedance spectra. As shown in **Figure 5b**, these correspond to a small semicircle in the high-frequency region and a large semicircle in the medium-frequency region in the Nyquist plot. This suggests that the four homogenized alloys share similar electrochemical corrosion mechanisms, with a small capacitive arc in the high-frequency region and a large capacitive arc in the medium-frequency region.

Studies have shown that the high-frequency region of the impedance spectrum is controlled by the kinetics of the electrode reaction (charge transfer process), the medium-frequency region is controlled by the diffusion of reactants or products of the electrode reaction, and the appearance of an inductive arc in the low-frequency region is due to localized corrosion or pitting corrosion on the alloy surface.[20,21] Generally, if an arc is present in the high-frequency region, it indicates that electron transfer is hindered, and the larger the arc radius, the slower the electron transfer rate. Conversely, a larger radius of the capacitive arc in the medium-frequency region indicates greater difficulty for charges to pass through the corrosion product film on the metal surface and form an electric double layer with the solution, thereby reducing the corrosion rate of the metal in the solution.[22] As seen in **Figure 8b**, the high-frequency arc radii of the five ho-

Table 3: Fitting results of the electrochemical impedance spectra for the homogenized alloys

Alloys	R_s/ $\Omega \cdot cm^2$	CPE_t		R_t/ Ω cm^2	CPE_f		R_f/ $\Omega \cdot cm^2$	R_l/ $\Omega \cdot cm^2$	L/ $H \cdot cm^2$
		Y_1/ $\Omega^{-1} \cdot cm^{-2} \cdot S^{-1}$	n_1		Y_2/ $\Omega^{-1} \cdot cm^{-2} \cdot S^{-1}$	n_2			
Mg-1Sn-0.6Ca	0.54	8.905E-007	0.91	7.427	7.076E-005	1	8.68	44.75	958
Mg-2Sn-0.6Ca	0.55	9.384E-007	0.97	8.9	7.253E-005	0.9	225	63.05	523.6
Mg-6Sn-0.6Ca	0.57	8.06E-007	0.99	8.905	9.001E-005	0.89	251.5	124.8	706.1
Mg-7Sn-0.6Ca	0.64	7.902E-007	1	7.508	5.692E-005	0.86	71.55	57.85	634

mogenized alloys are similar, with the Mg-1Sn-0.6Ca alloy exhibiting the smallest high-frequency capacitive arc radius and the lowest solution resistance of 0.54 $\Omega \cdot cm^2$, indicating that the Mg-1Sn-0.6Ca alloy has the best conductivity. Comparing the medium-frequency capacitive arc radii of the alloys, the order from largest to smallest is: Mg-6Sn-0.6Ca > Mg-2Sn-0.6Ca > Mg-7Sn-0.6Ca > Mg-1Sn-0.6Ca. A larger capacitive arc radius suggests that the accumulation of corrosion products and surface roughness result in a higher surface film resistance, thereby reducing the corrosion rate of the metal in the solution. This corresponds to the frequency-impedance trend in the Bode plot (**Figure 8c**), where a higher impedance |Z| value indicates a lower dissolution rate and better corrosion resistance. Thus, the homogenized Mg-6Sn-0.6Ca alloy exhibits the best corrosion resistance, while the Mg-1Sn-0.6Ca alloy shows the poorest corrosion resistance.

SEM scanning and area analysis were performed on the corrosion products of the homogenized alloys after 24 h of immersion, as shown in **Figure 6**. The results indicate that magnesium alloys with different compositions exhibit significant differences in corrosion behavior. These differences are primarily related to the microstructure, elemental distribution, and protective nature of the corrosion products.[23,24] From the SEM images, it can

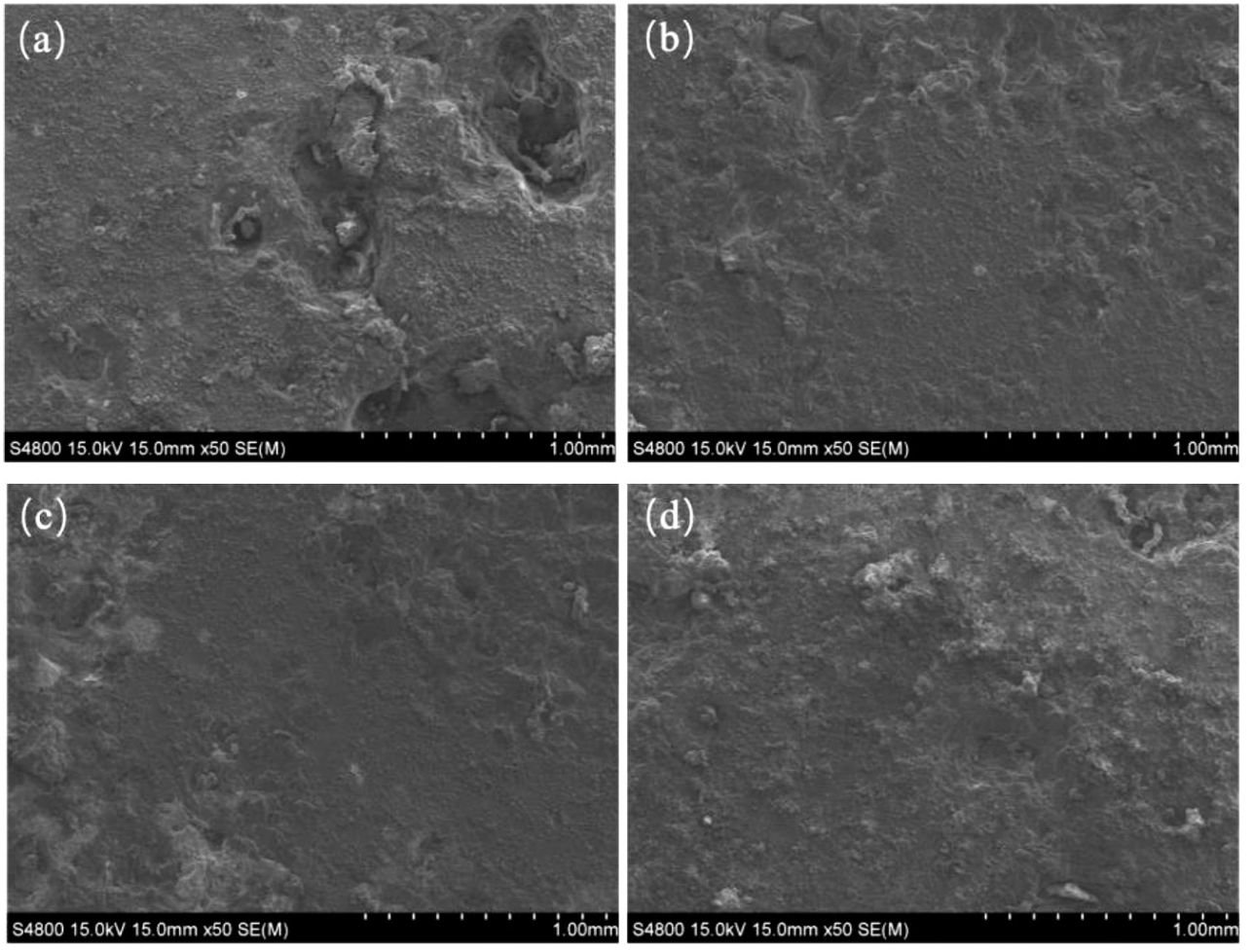

Figure 7: SEM images of the surface corrosion products of the homogenized alloys after 24 h of immersion: a), b) Mg-1Sn-0.6Ca; c), d) Mg-2Sn-0.6Ca; e), f) Mg-6Sn-0.6Ca; g), h) Mg-7Sn-0.6Ca

be observed that the surface of Mg-6Sn-0.6Ca is smooth, with no obvious corrosion pits, the least distribution of oxygen, and fewer corrosion products. This phenomenon may be attributed to the synergistic effect of Sn and Ca elements. Sn can form stable secondary phases (such as Mg_2Sn) in the magnesium matrix, which are uniformly distributed, effectively hindering the propagation of corrosion. Meanwhile, the addition of Ca further enhances the corrosion resistance of the alloy. Additionally, Ca and Sn can jointly form a protective oxide film, inhibiting further erosion by corrosive media. The surface of Mg-2Sn-0.6Ca shows corrosion pits, with relatively uniform elemental distribution and fewer corrosion products. Compared to Mg-6Sn-0.6Ca, the lower Sn content results in a reduced quantity of secondary phases (Mg_2Sn), weakening their inhibitory effect on corrosion. However, the presence of Ca still refines the grain structure and improves corrosion resistance to some extent, leading to relatively mild corrosion. The surface of Mg-7Sn-0.6Ca exhibits a few corrosion pits, with uneven elemental distribution and more corrosion products.

Although the higher Sn content promotes the formation of more Mg_2Sn secondary phases, excessive Sn may cause segregation of these phases at grain boundaries, leading to localized micro-galvanic corrosion and exacerbating corrosion non-uniformity. Furthermore, the uneven elemental distribution reduces the corrosion resistance in localized regions, resulting in more corrosion products. The surface of Mg-1Sn-0.6Ca shows severe corrosion, with numerous pits, uneven elemental distribution, and abundant corrosion products. Due to the low Sn content, the quantity of Mg_2Sn secondary phases is significantly reduced, leading to a substantial decline in corrosion resistance. At the same time, the effect of Ca is insufficient to compensate for the negative impact of low Sn content, making the alloy surface more susceptible to corrosion by the medium. The uneven elemental distribution further aggravates localized corrosion, resulting in the extensive formation of corrosion products.

Based on the elemental area scanning of the corrosion product layer (**Figure 7**), it can be observed that the corrosion products on the surfaces of the five alloys are primarily composed of high concentrations of O and Mg, with relatively low amounts of Sn and Ca. Therefore, it is inferred that the passive film formed on the alloy surfaces mainly consists of magnesium oxide or magnesium hydroxide, exhibiting high chemical stability and enhancing the corrosion resistance of the alloys.

Figure 8 shows the SEM images of the homogenized alloys after immersion in the 3.5 *w*/% NaCl solution for 24 h and removal of the corrosion products. From the low-magnification images, it can be observed that some deep corrosion pits on the matrix of the four alloys are likely regions with larger secondary phases or concentrated rare earth elements, where severe micro-galvanic corrosion has occurred. In **Figure 8a**, the corrosion pits are the largest, deepest, and most densely distributed, while in **Figure 8e**, the pits are the shallowest and least numerous. In **Figure 8c**, the pits are fewer and less connected, whereas in **Figure 8g**, the pits are more numer-

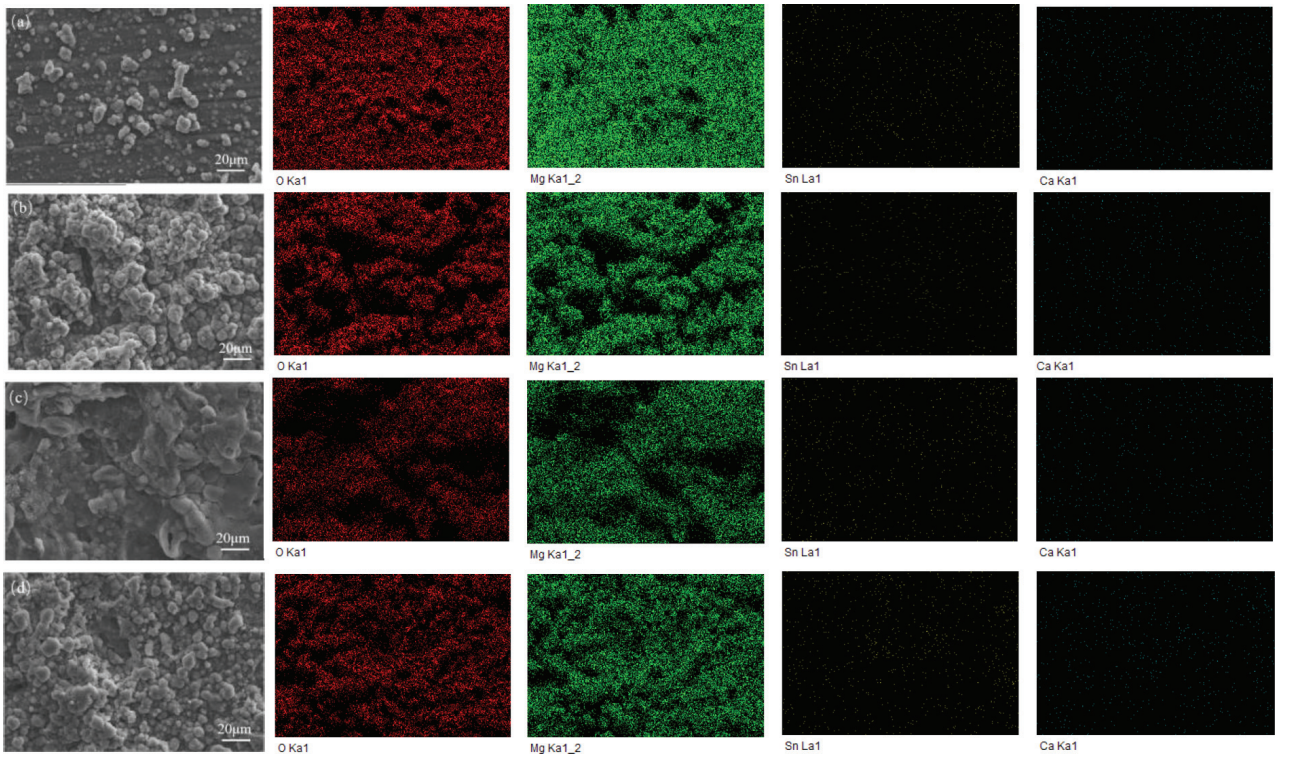

Figure 7: Elemental distribution maps of the surface corrosion products of the homogenized alloys after 24 h of immersion: a) Mg-1Sn-0.6Ca; b) Mg-2Sn-0.6Ca; c) Mg-6Sn-0.6Ca; d) Mg-7Sn-0.6Ca

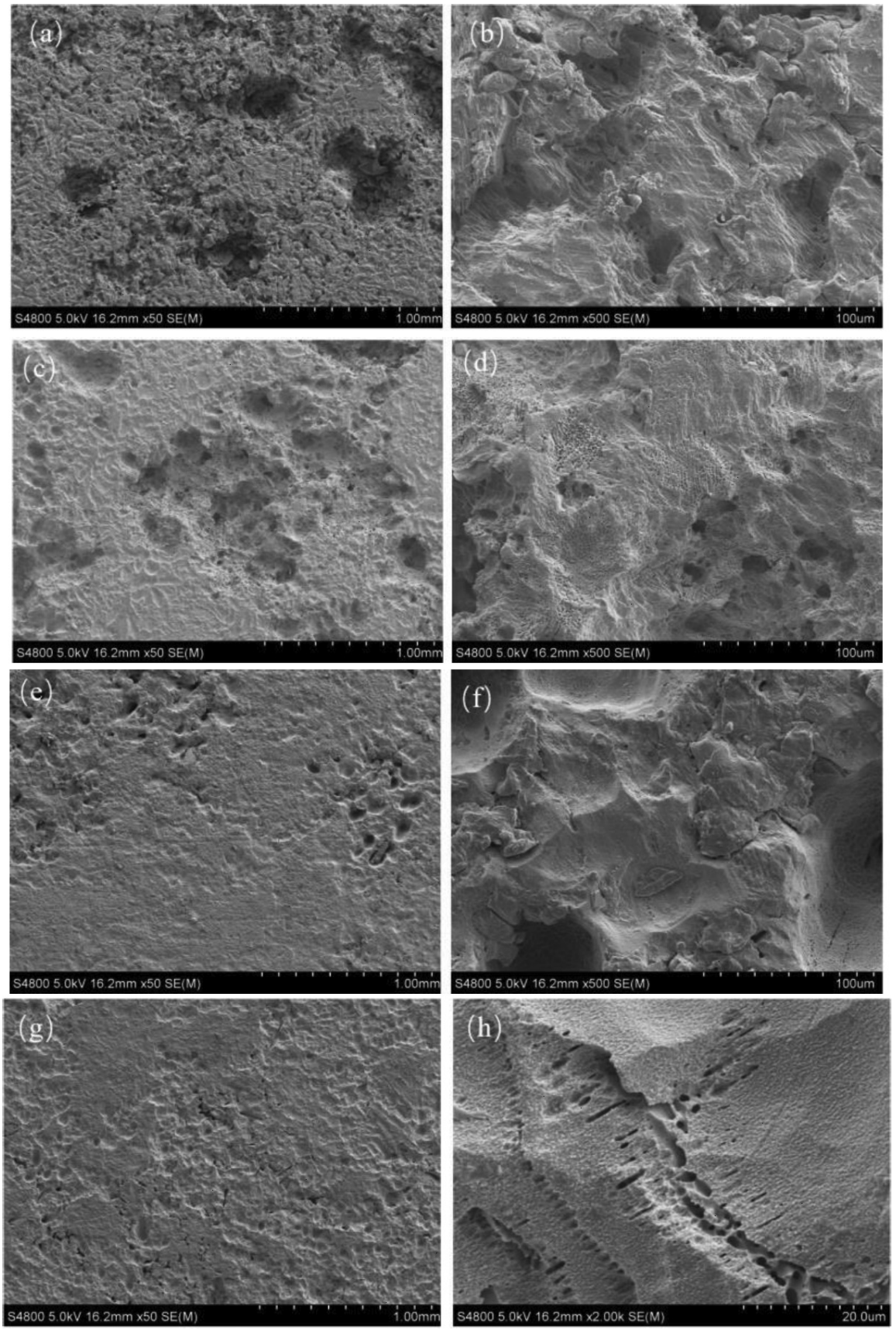

Figure 8: SEM images of the homogenized alloys after immersion in 3.5 *w*/% NaCl solution for 24 hours and removal of corrosion products: a), b) Mg-1Sn-0.6Ca; c), d) Mg-2Sn-0.6Ca; e), f) Mg-6Sn-0.6Ca; g), h) Mg-7Sn-0.6Ca

ous and dispersed. From the high-magnification images, it is evident that most of the secondary phases at the grain boundaries have dissolved or detached. **Figures 8b**, **8d**, **8f**, and **8h** show varying degrees of damage within the corrosion pits, with **Figure 8b** exhibiting a few cracks in the pits. Overall, the surfaces of the alloys display localized corrosion features. Among them, the Mg-6Sn-0.6Ca alloy retains some relatively intact surfaces with the least localized corrosion, while the Mg-1Sn-0.6Ca alloy exhibits the most severe localized corrosion and the largest corroded surface area. These results indicate that, among the four homogenized alloys, the Mg-6Sn-0.6Ca alloy has the best corrosion resistance, followed by Mg-2Sn-0.6Ca, then Mg-7Sn-0.6Ca, and finally Mg-1Sn-0.6Ca, which has the poorest corrosion resistance. These findings are consistent with the hydrogen evolution and weight loss experimental results.

4 CONCLUSIONS

In this study, the effects of the Sn content on the microstructure, distribution of secondary phases, and electrochemical corrosion behavior of Mg-xSn-0.6Ca (x = 1, 2, 6, 7) alloys were systematically investigated by adjusting the Sn content. The following conclusions were drawn:

(1) As the Sn content increases, the quantity and size of the Mg_2Sn and CaMgSn secondary phases in the alloys significantly increase. When the Sn content is 6 %, the Mg-6Sn-0.6Ca alloy forms an appropriate amount of secondary phases, effectively hindering the diffusion of corrosive media and significantly enhancing the corrosion resistance of the alloy.

(2) The corrosion resistance of the alloys initially improves and then deteriorates with increasing Sn content. The Mg-6Sn-0.6Ca alloy exhibits the best corrosion resistance, with hydrogen evolution and weight loss corrosion rates of 5.999 mm·year^{-1} and 9.346 mm·year^{-1}, respectively, which are significantly lower than those of the other alloys.

(3) Electrochemical test results show that the Mg-6Sn-0.6Ca alloy has the lowest self-corrosion current density (9.17 μA·cm^{-2}), further confirming its excellent corrosion resistance. Electrochemical impedance spectroscopy (EIS) analysis reveals that this alloy has a higher charge transfer resistance and surface film resistance, indicating that its corrosion product film provides better protection.

(4) The synergistic effect of Sn and Ca significantly improves the corrosion resistance of the alloys by refining the grain structure and forming stable secondary phases. However, excessive Sn content (such as, 7 %) may lead to the segregation of secondary phases at grain boundaries, causing localized micro-galvanic corrosion, thereby reducing corrosion resistance.

5 REFERENCES

[1] P. Jiang, C. Blawert, J. Bohlen, et al., Corrosion performance, corrosion fatigue behavior and mechanical integrity of an extruded Mg4Zn0.2Sn alloy, Journal of Materials Science & Technology, 59 (**2020**) 24, 107–116

[2] X. Wang, D. Xu, R. Wu, et al., What is going on in magnesium alloys?, Journal of Materials Science & Technology, 34 (**2018**) 02, 245–247

[3] B. L. Mordik, T. Ebert, Magnesium: Properties-applications-potential, Materials Science and Engineering: A, 302 (**2001**) 1, 37–45

[4] S. Zhang, X. Zhang, C. Zhao, J. Li, Y. Song, C. Xie, H. Tao, Y. Zhang, Y. He, Y. Jiang, Y. Bian, Research on an Mg-Zn alloy as a degradable biomaterial, Acta Biomaterialia, 6 (**2010**) 2, 626–640

[5] S. H. Cai, T. Lei, N. F. Li, F. F. Feng, Effects of Zn on microstructure, mechanical properties and corrosion behavior of Mg-Zn alloys, Materials Science and Engineering: C, 32 (**2012**) 8, 2570–2577

[6] C. Ke, M. S. Song, R. C. Zeng, Y. Qiu, Y. Zhang, R. F. Zhang, R. L. Liu, I. Cole, N. Birbilis, X. B. Chen, Interfacial study of the formation mechanism of corrosion resistant strontium phosphate coatings upon Mg-3Al-4.3Ca-0.1Mn, Corrosion Science, 151 (**2019**), 143–153

[7] X. Liu, J. Sun, F. Zhou, Y. Yang, R. Cang, K. Qiu, Z. Pu, L. Li, Y. Zheng, Micro-alloying with Mn in Zn-Mg alloy for future biodegradable metals application, Materials & Design, 94 (**2016**), 95–104

[8] H. R. Bakhsheshi-Rad, M. Abdellahi, E. Hamzah, A. F. Ismail, M. Bahmanpour, Modelling corrosion rate of biodegradable magnesium-based alloys: The case study of Mg-Zn-RE-xCa (x = 0, 0.5, 1.5, 3 and 6 wt %) alloys, Journal of Alloys and Compounds, 687 (**2016**), 630–642

[9] R. C. Zeng, L. Sun, Y. F. Zheng, H. Z. Cui, E. H. Han, Corrosion and characterisation of dual phase Mg-Li-Ca alloy in Hank's solution: The influence of microstructural features, Corrosion Science, 79 (**2014**), 69–82

[10] Z. Ding, L. Cui, R. Zeng, et al., Exfoliation corrosion of extruded Mg-Li-Ca alloy, Journal of Materials Science & Technology, 34 (**2018**) 09, 1550–1557

[11] Qiu Tianhang, Liu Ke, Lou Feng, Study on microstructure and mechanical properties of extruded Mg-12Gd-1Er-xSn-0.5Zr alloys, Modern Transportation and Metallurgical Materials, 4 (**2024**) 06, 95–102+112

[12] C. Wang, T. J. Luo, Y. T. Liu, Tao Lin, Y. S. Yang, Microstructure and mechanical properties of Mg-5Zn-3.5Sn-1Mn-0.5Ca-0.5Cu alloy, Materials Characterization, 147 (**2019**), 406–413

[13] Z. Yange, Comparative study on in vivo biosafety and osteogenic efficacy of Mg-Ca series alloys for fracture internal fixation, Chengde Medical University, 2024, DOI: 10.27691/d.cnki.gcdyx.2024.000018

[14] W. Cong, Hot deformation microstructure, properties, and residual stress of Mg-5Zn-3Sn-1Mn-0.5Ca-0.5Cu magnesium alloy, Northeastern University, 2020, DOI: 10.27007/d.cnki.gdbeu.2020.003044

[15] H. H. Li , Z. Z. Zhang, K. J. Wu, et al., Corrosion behavior of WC-304 cemented carbide in NaCl solution [J/OL], Journal of Materials Heat Treatment, 1–11 [2025-03-11], doi:10.13289/j.issn.1009-6264.2024-0298

[16] J. Tian, T. Tu, P. Dai, et al., Effect of homogenization annealing treatment on the microstructure of Mg-10Gd-4Y-1Zn-0.5Zr alloy, Foundry Technology, 44 (**2023**) 09, 843–848

[17] T. Y. Pan, L. B. Wang, Finite-element analysis of chemical transport and reinforcement corrosion induced cracking in variably saturated heterogeneous concrete, Journal of Engineering Mechanics – ASCE, 137 (**2011**), 334–345

[18] T. Huang, C. Xu, L. Yang, et al., Effect of Zr addition on microstructure and corrosion behavior of Mg-3Zn-1Y alloys, Journal of Chinese Society for Corrosion and Protection, 41 (**2021**) 2, 219–225

[19] T. Zhang, J. Zou, Z. Huang, Effect of rolling temperature on corrosion resistance of AZ61 magnesium alloy, Nonferrous Metals Science and Engineering, (**2022**), 1–9

[20] B. Deng, Q. F. Li, Y. Z. Wu, et al., Effect of secondary phases on the corrosion behavior of Mg-Zn-Zr alloy, Materials Protection, 54 (**2021**) 09, 48–53

[21] M. Yaghoobi, G. Z. Voyiadjis, V. Sundararaghavan, Crystal plasticity simulation of magnesium and its alloys: A review of recent advances, Crystals, 11 (**2021**) 4, 435

[22] C. Wang, H. Ning, S. Liu, et al., Enhanced ductility and strength of Mg-1Zn-1Sn-0.3Y-0.2Ca alloy achieved by novel micro-texture design, Scripta Materialia, 204 (**2021**), 114119